Collisionless multiphoton energy deposition and dissociation of SF_6

Jerry G. Black, Paul Kolodner, M. J. Shultz, Eli Yablonovitch, and N. Bloembergen

Gordon McKay Laboratory, Division of Applied Sciences, Harvard University, Cambridge, Massachusetts 02138

(Received 28 August 1978)

We have made careful absolute measurements of the collisionless multiphoton energy deposition in SF_6 for CO_2 laser pulses of varying duration and energy fluence. Likewise, we have also measured the absolute dissociation yields. An experimental plot of yield versus energy deposition shows that the energy distribution function is nearly thermal, becoming somewhat broader than thermal for the longer pulse durations. A "bottlenecking effect" of molecules in the discrete level region is held responsible for this smearing of the population distribution function.

I. INTRODUCTION

Since the first reports of isotope selectivity[1] in infrared-multiphoton-induced dissociation, the research effort in this field has grown tremendously[2]. Infrared-laser-induced chemical reaction has been shown to be a very general process, occuring in just about all polyatomic molecules. The most detailed attention has been directed toward sulfur hexafluoride, a molecule that is relatively easy to work with. The large quantity of spectroscopic and other data which has been collected on SF_6 permits us to begin to regard it as "the hydrogen atom" of the multiphoton dissociation problem.

Two of the key parameters of multiphoton dissociation are energy deposition and yield. The excitation energy left in the molecule after the laser pulse will, in general, be different for each molecule in the sample. Thus it makes sense to speak of an energy distribution function produced by the passage of the laser beam. The measured mean energy deposition will therefore tell us the mean of that energy distribution function. Only those molecules in the tail of the distribution function, with energy in excess of the activation energy, have a finite probability of dissociating. By measuring the reaction yield, we obtain an estimate of the fraction of molecules excited above the dissociation energy.

The two quantities, mean energy deposition and yield, measure two key parameters of the shape of the energy distribution function: namely, its mean and the fractional population in the tail. This gives us our first experimental information on the shape of the energy distribution prepared by multiphoton infrared excitation. In this article we shall report a series of unified measurements where both parameters are obtained together, with sufficient accuracy to specify the shape of the distribution function.

Section II of this paper will review some of the theoretical aspects of multiphoton excitation and dissociation. The experimental apparatus and techniques will be described in Sec. III and the results will be summarized and discussed in Sec. IV.

II. THEORY

One of the most important facts of multiphoton dissociation is that 30 or more infrared quanta are required to produce a reaction. This immediately provokes the theoretical question of what type of nonlinear process could be responsible for the absorption of 30 or more photons. While this problem was fraught with controversy at first, the weight of experimental information has now given us a clear answer. In this section we shall review the theory and the experimental evidence for it.

Although multiphoton excitation may be augmented or hindered by collisions, it does not depend upon them and is best observed under collisionless conditions. This was proven by experiments with molecular beams[3] and in gas cells[4] operating at very low pressure with ultrashort pulse irradiation.

In the early theoretical treatments coherent pumping effects among the low-lying discrete molecular levels were held to be important.[5] Such effects would be quite sensitive to the peak electric field of the laser wave, which is needed to overcome frequency mismatches with the discrete levels. Experimentally, in SF_6 it was shown[4] that the dissociation depended only weakly on peak power and instead was determined mainly by energy fluence. Such behavior is characteristic, not of the discrete levels, but rather of the higher-energy region of closely spaced vibrational levels, which has come to be called the quasicontinuum.[6]

The key property of the quasicontinuum is that at a sufficiently high density of states Fermi's Golden Rule becomes valid. In it the transitions are described in terms of intensity proportional rates,

and the full Schrödinger equation reduces to a set of rate equations. By contrast, in the discrete levels there appears to be no simplification or shortcut to a brute force solution of Schrödinger's equation.

The basic condition for the validity of Fermi's Golden Rule is that the transition rate should be neither too fast nor too slow:

$$[\hbar\rho(E)]^{-1} \ll \text{transition rate} \ll T_2^{-1}, \qquad (1)$$

where $\rho(E)$ is the density of available states and $\hbar/T_2$ is the width of the distribution of oscillator strength. When $\rho(E)$ is large enough, a rate equation description is permissible. This conclusion is especially useful in large polyatomics, where the thermal energy at room temperature is sufficient to boost most of the molecules into the quasicontinuum. In that instance, from the initial condition onward, we may use a rate equation description:

$$\frac{dW_n}{dt} = K_n^a I W_{n-1} + K_n^e I W_{n+1} - (K_{n+1}^a + K_{n-1}^e) I W_n$$

$$- K_n^{\text{diss}} W_n, \qquad (2)$$

where W_n is the probability of being in that group of states $n\hbar\omega$ above the starting level, K_n^a and K_n^e are absorption and stimulated-emission coefficients into that group, and K_n^{diss} is the reaction rate, which differs from zero only for those states above the activation energy. Ignoring K_n^{diss}, all the rates are proportional to the light intensity I, which may be divided from the right-hand side of Eq. (2) to show explicitly that the temporal evolution depends only on *intensity* $\times$ *time = energy fluence* (J/cm²).

This energy fluence scaling has been confirmed in number of experiments where the intensity and pulse duration were varied independently. Kolodner *et al.*[4] adjusted the infrared pulse duration in the range 0.5–100 nsec while keeping the energy fluence fixed. The fraction dissociated increased only 30%, even though the peak power increased by a factor of 200. The reaction yields depend very strongly on energy fluence but only weakly on peak power.

In a recent molecular-ion cyclotron resonance experiment, Beauchamp *et al.*[7] showed that the energy fluence scaling can, in some cases, extend to powers as low as 1 W/cm². Continuous wave irradiation for times of the order of 1 sec, and fluence of ~1 J/cm² produced dissociation of the species $[(C_2H_5)_2O]_2H^+$. In view of these experimental results, it is not unreasonable to regard the energy fluence scaling as experimentally confirmed over nine orders of dynamic range from 10^{-9}–1 sec.

A description of the infrared pumping in the quasicontinuum region requires a solution of Eq. (2). It should be emphasized, of course, that the molecules in the initial ensemble will start with an inhomogeneous distribution of internal vibrational energy, angular momentum, and translational momentum. This will lead to inhomogeneous broadening due to hot bands, rotation, and Doppler broadening. Each distinct initial state may experience slightly different absorption and stimulated emission coefficients in Eq. (2). In the approach that we shall adopt here, Eq. (2) will be solved under a number of simplifications. Inhomogenous effects of this type will be ignored.

It should be emphasized that the index n is not the quantum number of the driven normal mode, for example, the ν_3 mode in SF_6. While the quantum states in the discrete region tend to be readily identifiable in terms of specific normal modes of the molecule, each individual state of the quasicontinuum is generally a superposition of all modes. An up-transition in n could mean either an up or down transition in ν_3, depending on the individual states involved.

The absorption and stimulated emission coefficients in Eq. (2) represent up and down transitions as given by Fermi's Golden Rule. Since the matrix elements for an up and down transition are the same, the ratio of transition rates is given by the ratio of density of final states[8]

$$K_n^e / K_{n+1}^a = \rho[n\hbar\omega]/\rho[(n+1)\hbar\omega] \qquad (3a)$$

$$= \rho_n / \rho_{n+1}, \qquad (3b)$$

where ρ_n is the density of vibrational states at a vibrational energy level $n\hbar\omega$ above the starting state. The net absorption for a molecule in group n is the difference between the absorption and stimulated emission coefficients K_{n+1}^a and K_{n-1}^e. It may be expressed as a net absorption cross section σ_n,

$$\sigma_n \equiv (K_{n+1}^a - K_{n-1}^e)\hbar\omega. \qquad (4)$$

If the absorption coefficient σ_n as a function of internal vibrational energy $n\hbar\omega$ is known, then Eqs. (3) and (4) can be solved inductively to give all the unknown rates, K_n^a, and K_n^e as a function of n.

The absorption coefficients σ_n are best determined from experiment. It is known that the infrared spectrum of molecules changes only a little upon internal vibrational excitation. For example, the infrared spectrum of a molecule excited by thermal equilibrium heating[9] shows all the fundamental absorption bands. The bands are slightly broadened and shifted, but are otherwise not changed much. A similar conclusion arises from the infrared emission spectrum of molecules that

have experienced vibrational excitation by chemi-
activation.[10]

Whatever the observed change in absorption
cross section, it is due primarily to the broaden-
ing and anharmonic shifting of the bands. In this
respect SF_6 is unusual in having a very sharp infra-
red line with a strong anharmonic shift. Its cross
section at 944 cm^{-1} may drop by a factor of 20 up-
on vibrational excitation. In most molecules the
change in cross section is much less pronounced.[11]
The coefficients K_n^e and K_n^a may be deduced from
experimentally observed σ_n, where n is varied
thermally, by chemiactivation, or by infrared la-
ser excitation and double resonance probing.[12]
Nevertheless, for the sake of simplicity and gen-
erality we shall make the approximation that σ_n
does not depend too strongly on n, which is quite
well justified in almost all cases. Regarding σ_n
as a constant cross section σ, the solutions to
Eqs. (3) and (4) are easily obtained:

$$K_{n+1}^a = \frac{\sigma}{\hbar\omega} + K_n^a \frac{\rho_{n-1}}{\rho_n}. \tag{5}$$

For the sake of constructing a simple vibrational
density of states and for obtaining a general de-
scription that typifies most molecules, we assume
degenerate vibrational modes. With these assump-
tions Eq. (2) may be solved analytically, which is
of great advantage in understanding the basic pro-
cess. The assumptions may be relaxed, of course,
and the solutions could be obtained numerically on
a computer. The results will usually not differ
greatly from the analytic solution we shall present.

Assuming s degenerate vibrational modes, the
density of states is proportional to a combinatoric
factor:

$$\rho_n \propto \frac{(n+s-1)!}{n!(s-1)!} \tag{6}$$

and the ratio of density of states is given by

$$\frac{\rho_n}{\rho_{n+1}} = \frac{n+1}{n+s}. \tag{7}$$

By modelling the density of states in this way,
Eq. (5) can be written

$$K_{n+1}^a = \frac{\sigma}{\hbar\omega} + K_n^a \frac{n}{n+s-1}. \tag{8}$$

The principle of mathematical induction may be
used to solve Eq. (8). The absorption rate coeffi-
cient K_n^a into state n is given by

$$K_n^a = \frac{\sigma}{\hbar\omega} \frac{n+s-1}{s} \tag{9a}$$

The emission rate coefficient K_n^e into state n
may be obtained from Eq. (3):

$$K_n^e = \frac{\sigma}{\hbar\omega} \frac{n+1}{s}. \tag{9b}$$

For n below the dissociation limit, the analytic
solution of Eq. (2) turns out to be[13] none other than
a thermal distribution:

$$W_n = \frac{1}{Z} \exp\left(-\frac{n\hbar\omega}{\kappa T}\right) \frac{(n+s-1)!}{n!(s-1)!}, \tag{10}$$

where the partition function Z is given by

$$Z = \left[1 - \exp\left(-\frac{\hbar\omega}{\kappa T}\right)\right]^{-s}, \tag{11}$$

and the temperature as a function of time is given
by the energy conservation condition:

$$\frac{s\hbar\omega}{\exp(\hbar\omega/\kappa T) - 1} = \sigma \int^t I \, dt, \tag{12}$$

where the left-hand side of Eq. (11) is $s\hbar\omega$ times
the Bose-Einstein occupation number. Plugging
(9)–(12) into Eq. (2) shows that the thermal distri-
bution function (10) solves the equation. This con-
clusion is of great utility, since it suggests the
application of the well-developed machinery of
statistical thermodynamics to describe the molec-
ular behavior.

The Rice-Ramsperger-Kassel-Marcus (RRKM)
theory is the standard[14] statistical-mechanical
approach to unimolecular reactions. The reaction
rate $R(E)$ of a molecule containing energy E is
given by

$$R(E) = \tfrac{1}{2} k^+ \rho^+(E^+)/\rho(E) \tag{13}$$

where k^+, the barrier crossing rate, may be taken
as twice the rate of vibration, i.e., $k^+ = 2 \times 10^{13}$
sec^{-1}, and $\rho^+(E^+)$ is the density of states of the
activated molecule. In view of Eq. (6), the sim-
plified model of the density states which we are
using, our statistical model is actually the QRRK
(Quantum Rice-Ramsperger-Kassel) theory. In a
previous paper[15] we have shown that the difference
in results between the QRRK and RRKM models is not
very great. While the count of the number of states
appears crude, it is justified because it is like a one-
frequency grouping in the RRKM calculation where
Whitten and Rabinovitch[16] have shown that this
grouping is in good agreement with an exact count.

The density-of-states $\rho^*(E^+)$ available to the ac-
tivated complex is similarly calculated. We re-
quire that a minimum of m excitations be in the
mode corresponding to the reaction coordinate,
while the remaining $n-m$ excitations may be in
any of the s oscillators. The dissociation energy for
unimolecular reaction is taken as $m\hbar\omega$. The acti-
vated complex density of states is given by analogy
to Eq. (6) as

$$\rho^+(E^+=(n-m)\hbar\omega) \propto \frac{(n-m+s-1)!}{(n-m)!(s-1)!} .$$ (14)

For the case of SF_6 there are six equivalent S-F bonds that may be broken leading to a symmetry factor of 6 in Eq. (13). Thus the QRRK reaction rate is

$$R_n = 6A\frac{(n-m+s-1)!n!}{(n-m)!(n+s-1)!}$$ (15)

for a molecule containing n quanta of vibrational excitation and where $A \equiv \frac{1}{2}k^+$.

In this paper we shall restrict ourselves to the case of small fractional reaction yield per pulse. Then the dissociation terms on the right-hand side of rate equations (2) will have only a small effect on the temporal evolution of the overall distribution function. Thus we regard the infrared laser pumping as preparing a molecular distribution function over internal vibrational energy. After the laser pulse has passed a small fraction of all the molecules, namely, those in the tail end of the distribution function, will experience chemical reaction. An even smaller fraction of molecules may dissociate during the laser pulse, but their numbers will be too few to affect significantly the preparation of the distribution function. Therefore, in the low-yield limit we are justified in employing the thermal distribution function Eq. (10), which is the exact solution of the rate equations (2) in the absence of dissociation terms.

Most of the reactions occur after the laser pulse. Not every molecule with energy in excess of the dissociation energy will react. Dissociation must compete with some sort of collisional deactivation. The fractional dissociation from level n may be written

$$f_n = R_n/(R_n+D) ,$$ (16)

where D is the collisional deactivation rate with which R_n competes. The total fractional yield F is the convolution of the fractional dissociation with the distribution function:

$$F = \sum_n f_n W_n .$$ (17)

The final result of this theoretical calculation is a plot of F versus the internal vibrational temperature or, equivalently, versus the mean number of photons absorbed by the molecule. Detailed calculations and graphs of this type may be found in a previously published article.[15] In Sec. III the experimental results for F versus mean number of photons will be presented and compared with the above theory.

At this point it would be useful to review the assumptions and simplifications which went into the theory.

(i) The discrete level bottleneck[6] was ignored completely and the density of states was regarded as high enough to satisfy the left half of inequality (1). This is probably the most serious simplification, since we shall see in the experimental section that the energy fluence scaling is not exact. Presumably, the bottlenecking is an inhomogeneous effect, since it should depend on the initial state of the molecule. Therefore, we are also ignoring all inhomogeneous effects.

(ii) The infrared pumping rate is slower than T_2, the intramolecular dephasing and redistribution to the other modes of the molecule.[17] This seems well satisfied at the CO_2 laser pulse durations that were employed in these experiments.

(iii) The net absorption cross section remains constant as the molecule is excited. This ignores any anharmonic shifts in the absorption spectrum, which is a good approximation in most molecules. This is not well satisfied in SF_6 at 944 cm^{-1}, and it could lead to a bunching up of the distribution function as the less excited molecules absorb energy faster than the more excited molecules. This effect was first described in Ref. 18 as a narrowing of the distribution function in comparison with a thermal distribution.

(iv) The density of states is calculated from a degenerate oscillator model rather than the actual mode frequencies of the molecule. This does not lead to significant errors[15] in relation to experiment.

(v) The effect of dissociation on the distribution function prepared by the laser was ignored. This is justifiable for reaction yields small compared with unity.

(vi) The effect of collisional deactivation may be described by the phenomenological rate constant D. This approximation does not have a significant effect on the results.

(vii) The QRRK theory is used instead of the RRKM theory. Reference 15 shows that this does not affect the results significantly.

The main conclusion of the theory is that the molecular distribution is close to a thermal distribution function [Eq. (10)]. The departures from this formula arise mainly from approximations (i) and (iii). Simplification (iii) may be remedied by a computer calculation,[18] but assumption (i) is of a more fundamental nature. It is not completely understood why the discrete level bottleneck does not have an even stronger effect than that observed. In the past it has been modelled[6] by invoking a phenomenological bottlenecking fraction, although this tells little about the underlying principles. The experiments in this paper will permit us to estimate this effect. We shall see that assumption

(i) is primarily responsible for the discrepancies between theory and experiment.

III. EXPERIMENT

This section will describe two parallel series of experiments to explore the nature of energy deposition in single molecules of SF_6 and the resultant dissociation of the molecules. Deposition of laser energy is measured by the optoacoustical method,[6] essentially a calorimetric technique. Dissociation yield data are obtained by infrared spectroscopy before and after the gas has been irradiated with many laser pulses. The goal is to determine the internal vibrational energy distribution function produced by infrared laser pumping. The experimental technique, along with some novel mathematical procedures towards this end, will be detailed below.

The optoacoustical technique is ideally suited for absorption measurements in the type of samples encountered in this experiment. These must be gaseous at pressures sufficiently low to ensure the absence of collisions during irradiation. Spatial uniformity of irradiation must be maximized, even at higher fluences, where a narrow beam will spread as a result of diffraction. Thus the length of the sample is limited. At the high fluences encountered in this experiment, SF_6 absorbs 100 times more weakly at 944 cm^{-1} than it does in the small-signal regime. Here we have a thin, weakly absorbing sample with short path length. Accurate measurement of the transmission of this sample is impossible by ordinary techniques, since it differs from unity by typically 0.07%. This small absorption is easily detected by observing the momentary pressure increase due to the heating of the absorbing gas. Inherently a relative measurement process, it is calibrated absolutely by a standard transmission measurement carefully done with the same laser-beam geometry and same irradiation cell. Optoacoustical measurements of small concentrations of molecules is a well-established technique in air-pollution research.[19]

The experimental arrangement is shown in Fig. 1. Output from the Harvard short-pulse CO_2 oscillator-amplifier system[20] (grating-tuned at 944.2 cm^{-1}) was gradually focused by a 10-radius of curvature mirror, then further reduced by a BaF_2 lens placed in the focal plane of the mirror. The absorption cell (4.44-cm length, 1.9-cm diameter, NaCl windows) was located at the focus of this lens. Just prior to entering the lens, a NaCl beamsplitter directed 7% of the beam to a Ge:Au infrared detector. Fluence was varied by using CaF_2 attenuation flats with 0.5-mm inter-
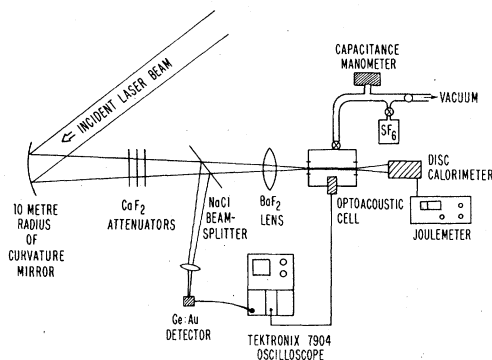

FIG. 1. Arrangement of apparatus for the energy deposition measurements described in the text. The incident CO_2 laser pulse is gradually focused by a 10-m radius of curvature mirror onto the optoacoustical cell. Further focusing, if required, is provided by a BaF_2 lens. Intensity of irradiation is controlled with CaF_2 attenuators. A Ge:Au detector monitors the laser pulse energy of each shot and is absolutely calibrated by frequent reference to the Joulemeter. Simultaneous photographs are taken of the Ge:Au signal and the optoacoustical microphone signal (see Fig. 2).

vals in thickness (transmission of 0.5-mm CaF_2 at 944 cm^{-1} is 82.5%). The aluminum cell was kept at a 10^{-4} Torr vacuum and filled for experiments with SF_6 (purchased from Matheson, no further purification). Pressure was monitored on a capacitance manometer (MKS Baratron). An electret microphone (General Radio No.1962-9602), cylindrical with 1.25-cm diameter, was located inside a vacuum housing integral with the cell such that the diaphragm was flush with the main bore of the cell (i.e., the microphone was 0.95-cm distant from the beam).

The Ge:Au detector was used as a linear detector to measure the energy of each laser pulse. The calibration of this reference arm was performed before each measurement session, using a Scientech Joulemeter placed after the evacuated cell. For each of several laser shots, one takes the ratio of the Joulemeter signal to the Ge:Au signal. Thus we have a reference arm calibration (joules incident per volt signal from Ge:Au). The absolute calibration of the Joulemeter itself was frequently checked by resistance substitution heating of the disk calorimeter. The output of the Ge:Au detector was displayed on one sweep of a Tektronix 7904 oscilloscope, and the microphone signal, after being amplified by a charge sensitive preamplifier (Ortec 124) was observed on a subsequent, slower sweep. Thus in one photograph (typical shot in Fig. 2) one can have a measurement of both the incident laser fluence and the resultant acoustical signal.
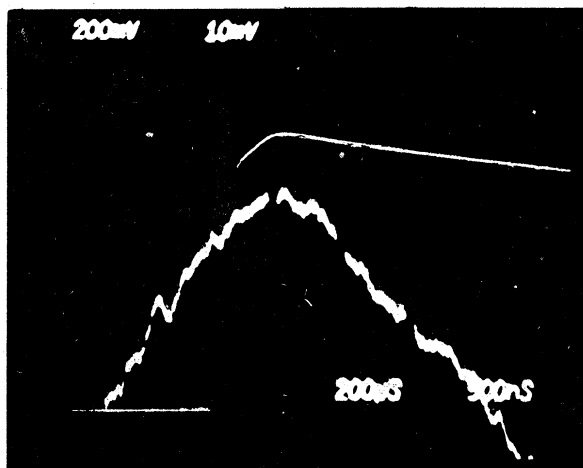
Three kinds of laser pulses were employed in

FIG. 2. Oscillograph of optoacoustical signal and integrated laser pulse energy. Lower trace: microphone signal (10 mV, 200 nsec/div.); Upper trace: Ge:Au signal (200 mV, 500 nsec/div.). Note that the upper trace does *not* display the temporal features of the laser pulse, but that the height of the trace is proportional to the pulse energy.

these experiments: long-pulse–multiple-axial mode, long-pulse–single-axial mode,[21] and short-pulse. The long pulses had 100-nsec full-width at half-maximum duration and the short pulses were of 500-psec duration. The transverse mode structure was single-mode Gaussian for all cases. For a fixed energy the multimode pulses exhibit intensity spikes that have approximately twice the peak power of the corresponding smooth single-mode pulses of the same energy. Only these 100-nsec multi-mode pulses were used in the dissociation experiments, this being the kind of pulse used by other laboratories for this purpose. The short pulses were produced by first truncating single-mode long pulses with a plasma shutter (optically triggered),[22] then further shortening them in a 3-m-long cell of hot CO_2 by optical free-induction decay followed by amplification.[23]

The optoacoustical experiment must be carefully performed to ensure linearity. As the experiment was done with gaseous samples at 0.121 Torr, one does not observe true sound waves, but rather a diffusive pressure pulse with temporal characteristics governed by the "soft" collisions with the cell wall. The "ringing" of the cell at its natural acoustical resonant frequency is only a small modulation at this low pressure. To be sure that the acoustical propagation is in the linear regime, the deposited heat should raise the temperature of the gas only a few degrees. Therefore, the beam area must be kept small with respect to the cross-sectional area of the cell. In this experiment the

ratio of areas was never larger than 0.003. Since the gas in the beam is being heated as high as 2000°K, the temperature of the gas striking the diaphragm is elevated only a few degrees. Also, the use of the small beam renders the measurement relatively free of dependence upon precise centering of the cell, which is not the case with larger beams. The acoustical signal is very sensitive to background pressure, so one must be sure that significant outgassing does not exist, or one must perform the measurements rapidly, before outgassing becomes a problem. A check to see whether room air produced an optoacoustical signal in our pressure range produced negative results even at the highest fluences. "Window click" was not observed.

The absolute calibration of energy deposition was done with the laser beam area defined by an aperture placed against the front surface of the cell window. In all other respects the optical setup was as shown in Fig. 1. This was done in order to achieve the best defined beam fluence profile. A 0.030-cm² aperture selected out the center of a beam focused to an area of 0.050 cm² by the 10-m radius of curvature mirror. The 0.030-cm² beam diffracts somewhat over the length of the cell, making the average beam area 0.035 cm². To allow for shot-to-shot fluctuations in the laser output power, the incident pulse energies were normalized with a Ge:Au photoconductive detector. Then ratios of the transmitted energy were taken with the cell filled to 4 Torr and with the cell evacuated. This gave the transmission T of the SF_6 in the cell:

$$T = \frac{\dfrac{\text{Joules on calorimeter}}{\text{Ge:Au detector signal}}\text{(filled cell)}}{\dfrac{\text{Joules on calorimeter}}{\text{Ge:Au detector signal}}\text{(empty cell)}}.$$

Note that the 500-psec pulses were used here, so we measure a collisionless absorption, even at 4 Torr. This added tremendous flexibility and permitted us to make a really accurate calibration. For each laser shot the fluence $\mathcal{I}$ is calculated from

$$\mathcal{I} = J\sqrt{T}/a, \tag{18}$$

where J is the incident energy obtained from the Ge:Au signal, calibrated as described previously, and $\sqrt{T}$ is the geometric mean of the cell transmission and corrects for the fact that the molecules at the entrance and exit windows are experiencing different fluence. The transmission was kept above 75% to ensure that the correction factor was small. The area a of the aperture was corrected slightly for diffraction, as indicated above. The average number $\langle n \rangle$ of photons

absorbed per molecule was calculated from the following formula:

$$\langle n \rangle = \frac{J(1-T)}{al\,N}, \tag{19}$$

where $l = 4.44$ cm was the length of the cell and N was the number density of molecules in the beam. After many such shots, which were averaged over statistical fluctuations, we obtained our standard absorption of short (500 psec) pulses: $\langle n \rangle = 16$ photons per molecule for a fluence of $\mathcal{J} = 0.8$ J/cm². All our optoacoustical measurements were calibrated to this point. Note again that the beam profile is much more uniform than that of a Gaussian beam, due to the aperture; there are no low intensity tails. The optoacoustical measurements were all done with Gaussian beams, but an exact deconvolution formula (see Appendix) was used to calculate the uniform fluence energy deposition.

The optoacoustical absorption data is shown in Fig. 3. These data were obtained using collimated beams with areas of 0.0041 and 0.010 cm², where the area of a Gaussian beam is taken as $\frac{1}{2}\pi\omega_0^2$. For obtaining data in the highest decade of fluence with the 500-psec pulses, it was necessary to use a different optoacoustical cell and a non-collimated focused beam. This cell is depicted in Fig. 4. Use of this cell was necessitated by the optical damage of the NaCl windows at intensities greater than 6 GW/cm² (500-psec pulse at 3 J/cm²). With beams focused to 0.0041 and 0.01 cm², the confocal parameters z_0 (the distance over which the beam area doubles) are 7.74 and 18.9 cm, respectively. The focused geometry in the baffled cell keeps the windows in a lower intensity region (45% of focal intensity), so short-pulse fluences up to 8 J/cm² are made possible, with a near-constant fluence in the central bore, where the acoustical signal is observed. Due to the smaller beam less total energy was deposited in the cell for a given fluence. The larger beam is necessary at lower fluences to keep the signal-to-noise ratio at an acceptable level. The baffled cell was difficult to use with the larger beam, so overlapping runs were done with both baffled and regular cells, with the results consolidated in Fig. 3.

The focal-beam areas mentioned above were measured by scanning across the beam with a Ge:Au detector masked by a 50-μm diameter pinhole. One such scan is shown in Fig. 5, along with a Gaussian fit to the measured intensity points. As is easily seen, the profile is very nearly an ideal Gaussian. An independent beam-width scan in the orthogonal direction was also done, revealing a slightly oval but still Gaussian
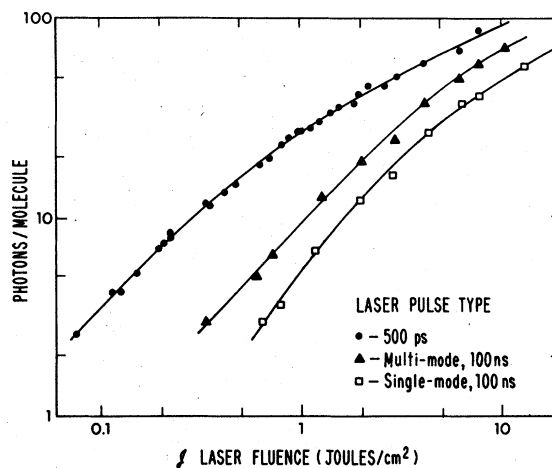

FIG. 3. Energy deposition in SF₆ measured optoacoustically with the incident CO₂ laser pulse having a Gaussian spatial profile. This is essentially the raw data, as opposed to Fig. 6, which corrects for the Gaussian spatial distribution of fluence. The three curves correspond to the three types of laser pulses employed in the experiment.

beam in both dimensions. Heretofore in the literature, a Gaussian beam was the standard intensity profile for irradiation of matter, with the peak intensity being used, for analytical purposes, as the average intensity. This is perfectly acceptable in linear systems; but where response is a nonlinear function of intensity or fluence, the fact that a Gaussian beam has a high-intensity center and wings that tail out to zero cannot be swept into an average so easily. It is shown in the Appendix that the exact fluence or intensity dependence of an additive function $f(I)$ can be deconvolved from the response function $f_G(I)$ measured as an average over a Gaussian beam by the simple formula:

$$f(I) = \frac{d(\ln f_G(I))}{d(\ln I)} f_G(I). \tag{20}$$

That is, multiplying $f_G(I)$ by its local logarithmic derivative yields the actual $f(I)$, the response
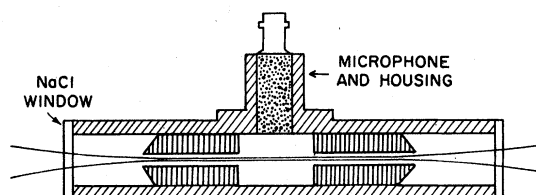

FIG. 4. Optoacoustical cell used to measure energy deposition at the highest fluences. Acoustical baffles prevent any signal from the molecules in the cone-shaped regions of the beam near the windows. The laser beam is well collimated in the space between the baffles. Total cell length is 17 cm, the diameter is 1.9 cm, and the central region is 2.5-cm long.
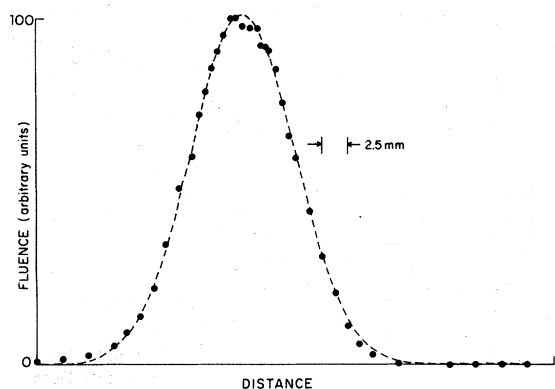
FIG. 5. Measured intensity profile of the incident laser pulses. The points represent the light intensity observed through a 50-μm pinhole translated across the beam. The curve is the best-fit Gaussian describing the position of the points on the graph. By this method we accurately determined that our laser beams were Gaussian, and measured the exact size of the beam.

function of the exact fluence I. Through this transformation the data in Fig. 3 become those of Fig. 6. For this purpose the smooth lines on Fig. 3 are least-squares fits of the data with the arbitrary functional form

$$\langle n_G(\mathcal{I}) \rangle = \frac{\alpha(\mathcal{I})^\beta}{(1 + \gamma \mathcal{I})^\delta},$$ (21)

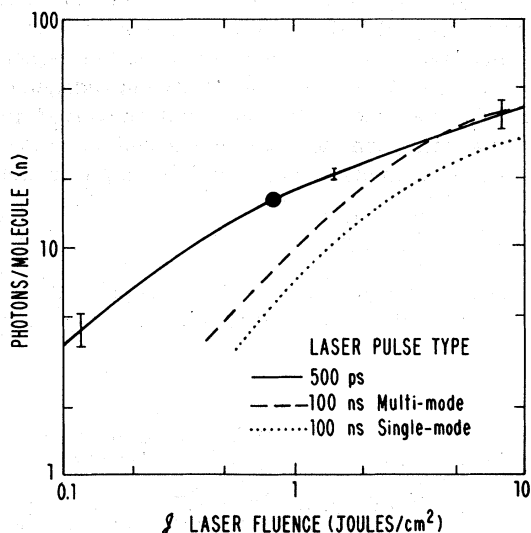where the values of α, β, γ, and δ are given in

FIG. 6. Energy deposition in SF_6, with the data deconvoluted by the method explained in the Appendix. The three curves correspond to the three curves of Fig. 3, but are reduced by Eq. (20) to represent the absorption per molecule in a laser beam of strictly uniform fluence. The solid dot is the absolute calibration point of the absorption data, to which all relative optoacoustical measurements are referenced. This point was painstakingly measured using conventional transmission techniques.

TABLE I. Parameters for arbitrary empirical fit [Eq. (21)] to experimental data.

Pulse type	α	β	γ	δ
500 $p$sec	58.04	1.15	1.96	0.725
100-$n$sec multimode	10.25	1.10	0.0302	2.35
100-$n$sec single mode	9.18	1.70	0.466	1.294

Table I for each of the three laser pulse types.

The absolute calibration of Fig. 3 was fixed by way of applying the 16 photons per molecule at 0.8 J/cm² point on Fig. 6, since that point was measured with a beam defined by a small aperture, not a full Gaussian beam. That point is marked by a round black dot on the 500-psec curve of Fig. 6. This amounts to running the Gaussian deconvolution Eq. (20) backwards to calibrate the raw data to appear as seen in Fig. 3. The difference between short- and long-pulse absorption at lower fluence is due to the former's greater peak power, enabling rapid excitation through the discrete lower states of SF_6. On the other hand, the longer pulses have lower peak power and tend to be bottlenecked in the discrete levels. At higher fluences the traces converge, as one would expect.

Using the given functional fits [Eq. (21) and Table I], one can generate the absorption cross section $\sigma = \langle n \rangle \hbar \omega / \mathcal{I}$ as a function of energy fluence for the three pulse types (Fig. 7). Similarly, one generates the incremental cross section $\sigma' = d \langle n \rangle \hbar \omega / d\mathcal{I}$ as a function of energy fluence (Fig. 8, depicted only for short-pulse case). These two forms of cross section have an important difference. The former is a sort of gross average absorption cross section of the molecule as it accepts photons, starting in its ground state, and is excited up the vibrational manifold. The latter is a measure of the cross section of the excited molecule, i.e., the ability of the hot molecule to accept another photon. Note that the data in Fig. 8 decrease more rapidly with increasing fluence than those of Fig. 7, since in the former the higher cross section at low fluence is not being averaged into the gross cross section. At low fluence, of course, the two graphs agree. The observed rapid decrease of cross section at 944 cm⁻¹ is consistent with the idea[9,17] that the molecular-absorption cross section is shifting and broadening with respect to the cold molecule's absorption. In Fig. 9 is shown the measured-absorption cross section as a function of vibrational temperature in the laser-heated molecule, compared with the absorption cross section of shock-tube-heated SF_6 (data taken from Ref. 9). Good
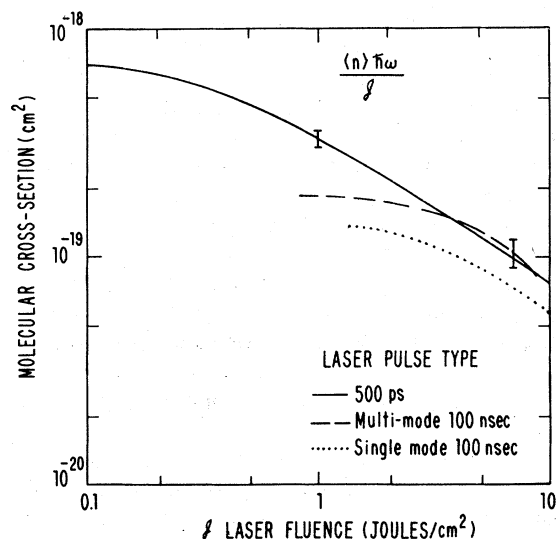
FIG. 7. Gross absorption cross section for SF_6 for each of the three laser pulse types. This data corresponds to uniform laser irradiation.

agreement with thermal behavior is seen in the cross section at the temperatures displayed in Fig. 9.

The dissociation experiment is performed by multiple-shot irradiation of the same sample cell. It is done at 0.121 Torr to exclude collisions during the laser pulses. The small signal transmission of the filled cell at the ν_3 mode of SF_6 was measured in an infrared spectrophotometer.
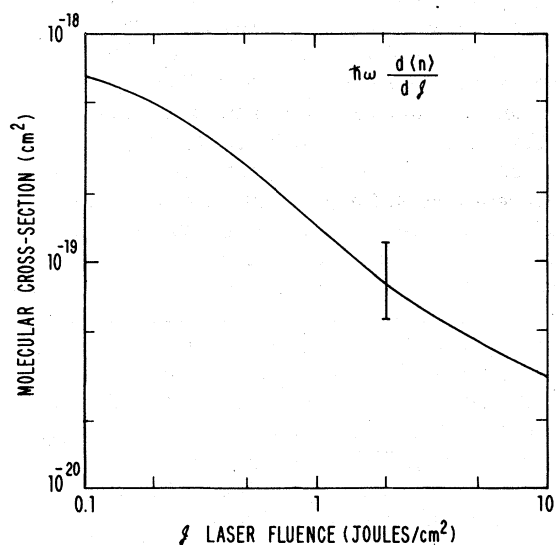

FIG. 8. Incremental absorption cross section for SF_6 irradiated by 500-psec laser pulses. This curve represents the molecular cross section for the excited molecules to incrementally absorb extra photons. The large error bar is due to the twice-differentiated nature of this data (see text).
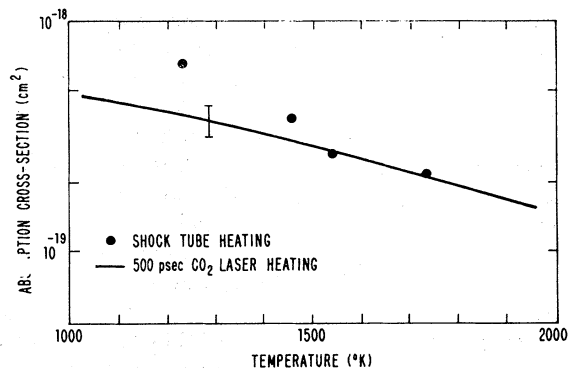

FIG. 9. Incremental absorption cross section plotted vs vibrational temperature. The temperature is derived from the number of photons absorbed by the quantum equipartition theorem. The points are taken from Ref. 9. The curve shows data in Fig. 8 replotted vs temperature.

After measuring the average pulse energy with the Joulemeter, the cell was placed in the beam for an irradiation consisting of 12–5000 laser pulses. Afterwards, the small signal ν_3 transmission was measured again. The fraction of SF_6 remaining undissociated is proportional to the ratio of the logarithms of the transmissions after and before the irradiation. Long-term shot-to-shot stability of the laser-pulse energy was checked by observing the output of the Joulemeter on a strip-chart recorder. After dissociation no reverse reaction is observed, in contradiction to Tal *et al.*[24] The fluorine and SF_5 radicals are quick to react with any impurity or with the cell wall. Both the SF_6 and the products are stable, even on the time scale of hours, as observed in the infrared spectra. One should avoid overexposing the sample, i.e., dissociating more than 25% of the SF_6, to ensure that the post-irradiation reaction milieu is not greatly altered over the course of a long exposure.

The reaction yield per shot was determined from the following formula:

$$F = (A'/aM) \ln (P_i/P_f) ,$$

where P_i and P_f are the initial and final partial pressures, A' and a are the cell and beam areas, respectively, and M is the number of laser shots of irradiation. The beam was a collimated Gaussian, and its area is taken as $a = \frac{1}{2}\pi\omega_0^2$, where ω_0 is the familiar Gaussian mode parameter. Since the reaction yield is a Gaussian averaged quantity, it was deconvolved using Eq. (20).

Comparing RRKM reaction theory to the dissociation experiment, the combined data are plotted in Fig. 10. Here the squares represent the dissociation yield for multimode 100-nsec pulse irradiation, with the corresponding number of photons

absorbed at the irradiation fluences at which the
dissociation was performed. The circles repre-
sent the same dissociation data, but with the pho-
ton number corresponding to 500-psec pulse
irradiation at the same fluence as the multimode
100-nsec radiation, which was used for the disso-
ciation. We did not repeat the dissociation ex-
periments with the 500-psec pulses, since
Kolodner et al.[4] had already shown that the yield
changed little over the full range of pulse dura-
tions.

Figure 10 is the main result of this paper. The
experimental points give information on the shape
of the distribution function, as discussed in Sec.
I. The theoretical curve was calculated on the
basis of the theory which had been outlined in
Sec. II. Namely, it is based on the assumption of
a thermal distribution function. In the theory, the
dissociation energy was taken as 94 kcal/mole,
or $m = 35$ photons, as recommended by Benson.[25]
The conclusions to be drawn from the theory and
experiment will be discussed in Sec. IV.

Let us close this section with an analysis of the
experimental errors. We estimate the uncertain-
ty in the optoacoustical data to be about 10%, re-
sulting almost entirely from the uncertainty in
the absolute absorption measurement. Since the
derived data, such as Figs. 6 and 7, involve
taking derivatives, the error is roughly doubled
for these curves. Figure 8 displays twice-differen-
tiated data, and thus is even more uncertain. Note,
for example, the error bars of Fig. 6. The error is
greater at the extremes, since the derivative of
the data is based on fewer data points.

The collisionless nature of the energy deposi-
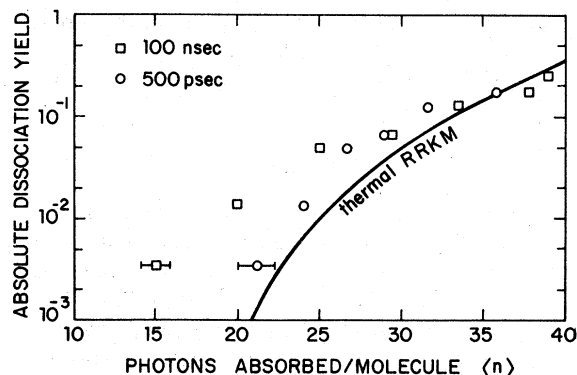tion was confirmed by using the transmission

FIG. 10. Dissociation probability per pulse as a func-
tion of the mean energy of excitation per pulse, $\langle n \rangle \hbar \omega$.
This graph gives information relating to the shape of the
energy distribution function produced by multiple photon
absorption. The experimental points for two pulse dura-
tions are compared with a theoretical curve (thermal
RRKM) based on the assumption of a thermal equilibrium
distribution of the same mean energy.

technique in a 1.25-m cell with the 100-nsec
pulses at pressures in excess of 0.121 Torr. At
a pressure of 0.35 Torr, the energy deposition
had increased only 10%. Extrapolating backward
shows that the additional energy deposition due to
finite pressure effects at 0.121 Torr was surely
less than 10%.

To ensure that the absolute calibration was not
affected by SF_6 molecules adsorbed on the win-
dows, the transmission experiments were re-
peated at constant pressure for cells of different
length. No window contribution was observed.

IV. DISCUSSION AND CONCLUSIONS

The experimental results presented in Sec. III
permit us to draw some definite conclusions re-
garding the theoretical model for multiphoton
pumping. In particular, it is interesting to test
the energy fluence scaling, which is the starting
point of the theory.

Figure 6 shows the energy deposited per mole-
cule by the different types of pulses. The absolute
calibration point is marked by the heavy black dot
on the 500-psec curve. It can be seen immediate-
ly by inspection of the curves that the energy
fluence scaling is not exact. The smooth 100-nsec
pulse deposits the least energy. A multimode
pulse of the same duration deposits about twice
as much energy. The 500-psec pulse deposits
much more energy at the low end, but converges
with the 100-nsec multimode pulse above $\mathcal{g} = 3$
J/cm². The differences are real, but they should
not be overemphasized. The peak power changes
by a factor of 200, while the energy deposition
increases by only a factor of 2. The fluence de-
pendence dominates the effects of peak power.

Since the energy fluence scaling should be ex-
act in the quasicontinuum, it is clear that the
discrete levels are still playing a role. However,
it is the discrete levels that are the most diffi-
cult to model. One would have to know the energy,
matrix elements, selection rules, and exact wave
function for all the levels. This is a very for-
bidding task. Especially sobering is the factor-
of-2 difference in energy deposition between the
multimode and single-mode pulses of the same
duration. Thus, small changes in the spectral
structure of the optical pulse are having a
noticeable effect on our results. Clearly, fre-
quency mismatches are occurring in the discrete
level region and are more readily overcome by
the spectrally broad multimode pulse than by
the spectrally narrow single-mode pulse.

It is the frequency mismatches that are re-
sponsible for the "bottlenecking effect" in the
discrete level region. In view of the noticeable

effect of small spectral changes, it is clear that the different initial starting states of the molecules in the room-temperature ensemble may behave very differently in regard to bottlenecking. Therefore, discrete level bottlenecking should be regarded as an inhomogeneous effect, which is different for the different molecules of the initial ensemble. This compounds the difficulty of modelling the discrete levels.

Most laser-chemistry experiments are performed with multimode pulses. This further increases the difficulty, since it would be necessary to analyze the multimode statistics of the laser pulses. Those statistical fluctuations cause differences from shot to shot and may explain some discrepancies in results between different laboratories.

In spite of the difficulties mentioned above, some general trends, at least, can be noticed. The bottlenecking effect is diminished at high laser powers. The large Rabi precession frequencies induced by the peak laser powers help to overcome the frequency mismatches in the discrete level region. The 500-psec laser pulses above 1 J/cm^2 produce a Rabi precession frequency >5 cm^{-1}, which is sufficient to overcome any frequency deficit which may occur. Similarly, the longer duration pulses experience less bottlenecking at the higher fluences. In fact, the multimode and 500-psec pulses produce essentially the same energy deposition above 3 J/cm^2.

In a previous paper[6] we suggested the following model to describe the bottlenecking. The molecules were divided into two classes, those that went directly to the quasicontinuum and the fraction f that remained permanently bottlenecked. The difference in energy deposition with respect to the 500-psec pulse was attributed entirely to the fraction bottlenecked in the discrete levels. Therefore

$$f = \frac{\langle n \rangle - \langle n' \rangle}{\langle n \rangle} , \qquad (22)$$

where $\langle n \rangle$ is the mean number of photons deposited by the 500-psec pulse and $\langle n' \rangle$ is the number deposited by the longer pulses. For the multimode pulse the fraction f is one-half at 1 J/cm^2, going down to zero at higher fluences.

This model should be regarded as an approximation, for there is no reason to believe that the molecules divide neatly into two groups. In general, there will be a continuous variation in molecular behavior. The bottlenecking should slow the entry into the quasicontinuum, smearing the distribution function downward in an inhomogeneous way, i.e., differently for each starting state.

Our basic experimental information about the

distribution function is in Fig. 10. The vertical axis measures population in the tail of the distribution, while the horizontal axis measures $\langle n \rangle$, the mean of the distribution. The experimental points, which are plotted for both 500- and 100-nsec pulses, are compared with a curve derived from a thermal distribution function. It should be emphasized that there are no adjustable parameters in the theory. Indeed, the only parameter that goes into the theory is the dissociation energy, which is known[25] independently.

The experimental points for the multimode 100-nsec pulse fall to the left of the thermal curve, indicating a long tail to the distribution in relation to its center of gravity. This is clearly the effect of bottlenecking, which holds back the mean energy deposition, while not retarding those molecules which enter the quasicontinuum immediately. For the 500-psec pulses the bottlenecking is negligible and the points agree well within experimental error with the theoretical thermal curve. On the other hand, the single mode 100-nsec pulses deposit far less average energy due to severe bottlenecking. They would fall far to the left, off the graph, and not agree at all well with a thermal distribution due to the dominant influence of the discrete level bottleneck.

An important point should be made in regard to the effect of collisions on the observed yield. The infrared multiphoton pumping process is collisionless because of the short laser pulses, but most of the chemical reactions occur after the pulse has passed. Collisions afterward may affect the shape of the distribution function. They surely do, but the net effect of the up and down transitions induced by collisions is to make the distribution more thermal. In our case, it would reduce the excess population in the tail and bring about the collisional deactivation. This effect was described by the rate constant D in Sec. II of this paper.

Therefore, our basic conclusion is that infrared multiphoton pumping by 500-psec pulses in SF$_6$ produces an energy distribution close to thermal. Multimode 100-nsec pulses cause the distribution to depart from a thermal one by being smeared out, with a long tail in relation to its mean. These experimental observations differ from the predictions of Grant *et al.*[18] They employed a computer solution to overcome approximation (iii), which was made in the theory of Sec. II. Because of the falling cross section as seen in Fig. 9, the distribution will tend to bunch up and become narrower than a thermal distribution. Unfortunately, their computer solution ignored the effects of bottlenecking, which completely dominate the narrow-

ing that they were predicting. For 100-nsec pulses the distribution is broader than thermal due to bottlenecking. For 500-psec pulses the distribution is close to thermal, but the data are not accurate enough to see the discrepancy which Grant et al.[18] predicted.

In an experimental paper Ham et al.[26] measured the slope of the yield curve of Fig. 10 at one point near threshold. They claimed that the slope was too steep for a thermal distribution. The coordinates at which they measured the slope may fall below the bottommost data point on our graph; however, it does not necessarily disagree with our observations. Nevertheless, their measurement is in doubt because the authors of Ref. 26 were using a beam consisting of multiple spatial modes, which makes it impossible to interpret their results accurately. Even if they had used a Gaussian beam, it would still have been necessary to deconvolute the data spatially using Eq. (20). Therefore, that measurement cannot be directly compared with our data.

In conclusion, accurate measurements of energy deposition and yield permit a direct experimental determination of the shape of the energy distribution function produced by infrared-multiphoton pumping. The distribution function is close to thermal, becoming broader as a result of bottlenecking among the discrete levels. At present we do not have a realistic theory for the bottlenecking effect, and this remains a major challenge in our understanding of the details of infrared-multiphoton chemistry.

APPENDIX

In this paper we have measured local additive quantities such as energy deposition per molecule and dissociation probability per molecule. These local additive quantities are observed as a spatial average over a Gaussian beam. We are fortunate that an exact deconvolution formula

exists and we derive it here.

Let $f(I)$ be the local additive parameter that is a function of the local laser intensity I. We actually measure $f_G(I_G)$ which is the Gaussian spatially averaged form of f

$$f_G(I_G) \equiv \frac{1}{\pi\omega_0^2/2} \int_0^\infty f[I(r)]2\pi r \, dr \,, \qquad (23)$$

where $I(r) = I_G \exp(-2r^2/\omega_0^2)$ is a Gaussian intensity distribution with a radius at the beam waist of ω_0 and r is the radial coordinate in a plane. Noticing that $dI/I = d(2r^2/\omega_0^2)$, a change of variables may be made in formula (23):

$$f_G(I_G) = \int_0^{I_G} f(I) \frac{dI}{I}. \qquad (24)$$

Differentiating both sides of Eq. (25) with respect to I_G yields

$$\frac{df_G(I_G)}{dI_G} = \frac{f(I_G)}{I_G}, \qquad (25)$$

Changing dummy variables and rearranging terms gives

$$f(I) = I \frac{df_G(I)}{dI}. \qquad (26)$$

Expressing (26) in terms of a logarithmic derivative gives the mathematical form shown in Eq. (20). The derivation is equally valid for intensity or energy fluence. The only requirement is that the beam be Gaussian. A more complete set of Gaussian spatial deconvolution formulas will be published in a forthcoming paper.[27]

[1]R. V. Ambartsumian, V. S. Letokhov, E. A. Ryabov, and N. V. Chekalin, JETP Lett. 20, 273 (1974); J. L. Lyman, R. V. Jensen, J. Rink, C. P. Robinson, and S. D. Rockwood, Appl. Phys. Lett. 27, 87 (1975).
[2]N. Bloembergen and E. Yablonovitch, Phys. Today 31, 23 (1978).
[3]M. J. Coggiola, P. A. Schulz, Y. T. Lee, and Y. R. Shen, Phys. Rev. Lett. 38, 17 (1977).
[4]P. Kolodner, C. Winterfeld, and E. Yablonovitch, Opt. Commun. 20, 119 (1977).
[5]N. Bloembergen, C. D. Cantrell, and D. M. Larsen, in Tunable Lasers and Applications, edited by A. Mooradian, T. Jaeger, and P. Stokseth (Springer, New York,

1976).
[6]J. G. Black, E. Yablonovitch, N. Bloembergen, and S. Mukamel, Phys. Rev. Lett. 38, 1131 (1977).
[7]R. L. Woodin, D. S. Bomse, and J. L. Beauchamp, J. Am. Chem. Soc. 100, 3248 (1978).
[8]E. Merzbacher, Quantum Mechanics (Wiley, New York, 1961).
[9]A. V. Nowak and J. L. Lyman, J. Quantum Spectrosc. Radiat. Trans. 15, 1945 (1975).
[10]J. G. Moehlmann and J. D. McDonald, J. Chem. Phys. 62, 3052 (1975).
[11]J. F. Figueira (private communication).
[12]W. Fuss, J. Hartmann, and W. E. Schmid, Appl. Phys.

15, 297 (1978).

[13]E. W. Montroll and K. E. Shuler, J. Chem. Phys. 26, 454 (1957).

[14]P. J. Robinson and K. A. Holbrook, *Unimolecular Reactions* (Wiley, New York, 1972).

[15]M. J. Shultz and E. Yablonovitch, J. Chem. Phys. 68, 3007 (1978).

[16]G. Z. Whitten and B. S. Rabinovitch, J. Chem. Phys. 38, 2466 (1963).

[17]E. Yablonovitch, Optics Lett. 1, 87 (1977).

[18]E. R. Grant, P. A. Schulz, Aa. S. Sudbo and Y. T. Lee, Phys. Rev. Lett. 40, 115 (1978).

[19]P. D. Goldan and K. Goto, J. Appl. Phys. 45, 4350 (1974).

[20]H. S. Kwok and E. Yablonovitch, Rev. Sci. Instrum. 46, 814 (1975).

[21]A. Gondhalekar, E. Holzhauer and N. R. Heckenberg, Phys. Rev. A 46, 229 (1973).

[22]H. S. Kwok and E. Yablonovitch, Opt. Commun. 21, 252 (1977).

[23]E. Yablonovitch and J. Goldhar, Appl. Phys. Lett. 25, 580 (1974); H. S. Kwok and E. Yablonovitch, Appl. Phys. Lett. 30, 158 (1977).

[24]D. Tal, U. P. Oppenheim, G. Koren and M. Okon, Chem. Phys. Lett. 48, 67 (1977).

[25]S. W. Benson, Chem. Reviews 78, 23 (1978).

[26]M. Rothschild, W.-S. Tsay and D. O. Ham, Opt. Commun. 24, 327 (1978).

[27]P. Kolodner, H. S. Kwok, J. G. Black and E. Yablonovitch, Opt. Lett. 4, 38 (1979).